Full Length Article

A detailed investigation of MnO$_2$ nanorods to be grown onto activated carbon. High efficiency towards aqueous methyl orange adsorption/degradation

Eleonora Pargoletti [a,b,*], Valentina Pifferi [a,b], Luigi Falciola [a,b], Gianluca Facchinetti [a], Andrea Re Depaolini [c], Enrico Davoli [c], Marcello Marelli [d], Giuseppe Cappelletti [a,b]

[a] *Università degli Studi di Milano, Dipartimento di Chimica, via Golgi 19, 20133 Milano, Italy*
[b] *Consorzio Interuniversitario Nazionale per la Scienza e Tecnologia dei Materiali (INSTM), via Giusti 9, 50121 Firenze, Italy*
[c] *IRCCS Istituto di Ricerche Farmacologiche "Mario Negri", Via La Masa 19, 20156 Milano, Italy*
[d] *CNR-ISTM/ISTeM, via Fantoli 15/16, 20138 Milan, Italy*

ARTICLE INFO

ABSTRACT

Herein, we report a one-pot wet chemical method adopted to synthesize *ad hoc* MnO$_2$ nanoparticles. By varying both the manganese salt precursors (*e.g.* sulphate or chloride) and the oxidizing agents (*e.g.* ammonium persulphate, potassium permanganate or potassium bromate), we succeeded in tailoring MnO$_2$ structural, morphological and surface features. Hence, owing to nanopowders peculiar properties, they were exploited as adsorbents for aqueous Methyl Orange (MO) removal. Particularly, novel MnO$_2$ nanorods (from manganese sulphate and potassium bromate, namely MS_Br) showed the highest removal efficiency probably due to both its polymorphic composition and its highest percentage of pores with diameter under 20 nm. Then, this powder was grown on Activated Carbon (AC40, sample MS_Br@AC40) pellets to either enhance its adsorption properties or to facilitate the adsorbent removal at the end of the kinetic test. Novel MS_Br@AC40 shows superior MO removal capabilities, achieving the almost total pollutant disappearance, thanks to the synergistic adsorption/oxidation features between carbon (high surface area, *i.e.* 1200 m^2 g^{-1}) and MnO$_2$. By means of HPLC-MS on eluates, we also managed to investigate MS_Br and MS_Br@AC40 degradative power towards MO molecules, thus leading to a novel degradation pathway. Finally, the adsorbent regeneration capability has been evaluated, showing very promising results.

© 2018 Elsevier B.V. All rights reserved.

1. Introduction

Due to the rapid pace of global industrialization, the contamination of water resources has largely occurred [1–3]. Specifically, organic dyes are used in a wide range of industries, such as textiles, dying, leather, paper and they are one of the main water pollutants with severe environmental impact [4,5]. Moreover, the synthetic origin and complex aromatic molecular structures of these pollutants make them very stable and resistant to biodegradation. Particularly, Methyl Orange (MO) is a good representative of the aromatic azo-dyes and it constitutes about half of the total world dye market [6]. Furthermore, MO compounds are recognized as potential carcinogens [6,7] and, therefore, the treatment of wastewater containing them, prior to disposal, is becoming more and more urgent [8,9].

A variety of research studies have been recently carried out in order to remove/degrade MO from wastewaters [10–14]. Many technologies, such as chemical oxidation [15], photochemical/ultrasonic degradation [16,17], reverse osmosis [18] and flotation [19] have been exploited. Among them, adsorption is one of the most effective methods, due to its easy operation, low cost, availability of a wide range of adsorbents and, above all, because it is a non-destructive technology [20–24]. The most common used adsorbent for wastewater treatment system is bare activated carbon, owing to its large specific surface area [21]. However, the capability of carbon material to unspecifically adsorb all kinds of pollutant molecules (both dyes and organic species) has led to use it in the final step of the removal treatment [25].

Hence, among various available materials, metal oxides have potential applications in water treatment due to their high surface area and low regeneration costs [9]. In particular, nanosized manganese dioxide (MnO_2) is a multifunctional material, which has been broadly applied in the areas of electrocatalysis [26,27] and supercapacitors, as well as in the adsorption technology [9,28]. Furthermore, MnO_2 nanomaterials may also offer efficient and innovative solutions for organic pollutant degradation. Indeed, manganese dioxide can grow in more than 20 different polymorphs (having layered or tunneled structures) characterized by multivalent nature and nonstoichiometric compositions, which can lead to both high adsorption degree and great oxidative degradation power [9,29]. However, manganese oxides suffer from the low electron transfer performance and the small surface area [30]; hence, in order to overcome these issues, a MnO_2 growth onto Activated Carbon (AC) support could be performed, achieving composites characterized by enlarged surface area and great adsorption capabilities [31–33]. Indeed, the possibility to combine different materials to produce innovative composite with enhanced performances with respect to the precursors has brought important results in many research fields [34–36].

In this context, we report herein a deep investigation of novel hydrothermal syntheses of MnO_2 nanoparticles with peculiar physico-chemical properties. Indeed, by varying the starting manganese salt precursors and oxidizing agents, *ad hoc* MnO_2 nanorods with different structural and surface features, to be applied in the wastewater treatment, have been prepared. All the synthesized nanopowders have been used as methyl orange adsorbents and a further comparison among their adsorption capabilities has been made. Further, the most performing powder was grown on Activated Carbon (AC) to enhance its removal properties. Then, either pure or activated carbon-based composite were deeply studied on their adsorption/oxidation power and, since no literature is available about the complex MO degradation pathway by MnO_2 and MnO_2@AC, we hypothesized a possible mechanism exploiting the HPLC-MS on eluates. Finally, the adsorbent regeneration capability has been evaluated, showing very promising results.

2. Material and methods

All the chemicals were of reagent-grade purity and were used without further purification; doubly distilled water passed through a Milli-Q apparatus was utilized. All the reagents used were purchased from Sigma-Aldrich.

2.1. Synthesis of MnO_2 nanoparticles

In this work, we followed the one-pot hydrothermal procedure already optimized in our laboratory [27,37]. Herein, we adopted stoichiometric manganese sulphate monohydrate ($MnSO_4 \times H_2O$) or manganese chloride tetrahydrate ($MnCl_2 \times 4H_2O$) as the salt precursors, and ammonium persulphate (($NH_4)_2S_2O_8$), potassium permanganate ($KMnO_4$) or potassium bromate ($KBrO_3$) as the oxidizing agents. No further calcination steps were required, since all the synthesized nanopowders have shown a high degree of crystallinity (see in the following).

Samples were labeled as MX_Y according to either the salt precursor (X = S for manganese sulphate monohydrate or Cl for manganese chloride tetrahydrate) or the oxidizing agent (Y = N for ammonium persulphate, K for potassium permanganate or Br for potassium bromate) used (see Table 1).

Pellet Activated Carbon (type Ceca AC40, from Arkema Group, inset of Fig. S1a) was used in this study.

As concerns the composite powder, MS_Br was chosen to be grown on the carbon support thanks to its attested superior

Table 1
Mn^{2+} precursors and oxidizing agents adopted in the synthesis.

Sample	Precursor	Oxidizing agent
MS_N	$MnSO_4$	$(NH_4)_2S_2O_8$
MS_K	$MnSO_4$	$KMnO_4$
MS_Br	$MnSO_4$	$KBrO_3$
MCl_K	$MnCl_2$	$KMnO_4$

adsorption/degradation capacities (sample labeled as MS_Br@AC40). Hence, the analogous synthetic route was adopted, except for the addition of the activated carbon pellets in the flask containing the manganese salt solution, with a salt:AC40 weight ratio of 4:1.

2.2. Sample characterizations

X-ray Powder Diffraction (XRPD) analyses were performed on a Philips PW 3710 Bragg-Brentano goniometer equipped with a scintillation counter, 1° divergence slit, 0.2 mm receiving slit and 0.04° soller slit systems. We employed graphite-monochromated Cu Kα radiation (Cu $K_{\alpha 1}$ λ = 1.54056 Å, $K_{\alpha 2}$ λ = 1.54433 Å) at 40 kV × 40 mA nominal X-rays power. Diffraction patterns were collected between 20° and 90° with a step size of 0.1° and a total counting time of about 1 h. A microcrystalline Si-powdered sample was used as a reference to correct for instrumental line broadening effects.

Scanning Electron Microscopy (SEM)/Energy Dispersive X-ray spectroscopy (EDX) were carried out using a LEO 1430 Microscope (100k magnification, 5 nm resolution) coupled with Hitachi ED3000 spectrophotometer.

Transmission Electron Microscope (TEM) analyses were performed on LIBRA 200 EFTEM (Zeiss) instrument operated at 200 kV accelerating voltage. The TEM grids were prepared dropping the dispersed suspension of nanoparticles in isopropanol onto a holey-carbon supported copper grid and drying it in air at room temperature overnight.

The BET surface area was determined by a multipoint BET method using the adsorption data in the relative pressure (p/p_0) range of 0.05–0.20 (Coulter SA3100 apparatus). Desorption isotherms were used to determine the total pore volume using the Barrett-Joyner-Halenda (BJH) method.

In order to investigate Mn oxidation states in the as-prepared manganese dioxide nanoparticles, Cyclic Voltammetry (CV) analyses were carried out by using MnO_2-Glassy Carbon (MX_Y−GC) electrodes (*i.e.* diamond powder polished GC was modified by 20 μL drop casting of 1 mg mL^{-1} MnO_2 nanoparticles suspension in dimethylformamide). The electrochemical measurements were performed in a conventional three-electrode cell using a platinum wire as counter electrode, a Saturated Calomel Electrode (SCE) as reference electrode and the MX_Y−GC as working electrode. An acetate buffer (pH 4) was utilized as the supporting electrolyte. The CVs were recorded at room temperature by using an Autolab PGStat30 (Ecochemie, The Netherlands) potentiostat/galvanostat controlled by NOVA 2.0 software for data acquisition. A step potential of 0.005 V and a scan rate of 0.1 V s^{-1} were adopted, in the potential range between −1.0 and +1.7 V (*vs* SCE). For the same purpose, X-ray Photoelectron Spectroscopy (XPS) analysis was carried out using a Mprobe apparatus (Surface Science Instruments). The source was the monochromatic Al Kα radiation (1486.6 eV); a spot size of 200 × 750 mm and a pass energy of 25 eV were used. The 1s level of hydrocarbon-contaminant carbon was taken as the internal reference at 284.6 eV. The accuracy of the reported binding energies (B. E.) can be estimated to be around 0.2 eV and the resolution is equal to 0.74 eV.

2.3. Methyl Orange removal tests

The Methyl Orange (MO) adsorption/removal capability was achieved by mixing 150 mL of MO aqueous solution (100 mg L^{-1}) and 75 mg of pure manganese dioxide nanopowders or carbon-based composite (500 mg L^{-1}, 5:1 weight proportion absorbent: MO molecules). All the experiments were carried out at room temperature, at spontaneous pH ($\sim$3 for all the samples) and dark conditions, under vigorous stirring both to maintain a good dispersion of the MnO$_2$ nanopowders and to assure interaction between the adsorbent material and the dye. Indeed, the point of zero charge (pzc) of all the synthesized MnO$_2$ nanopowders is lower than 3, whereas pK$_a$ of MO is around 3.5 [38]. Thus, at pH $\sim$ 3 dye molecules and nanoparticles show a slightly neutral and negative charge, respectively. So, under these conditions, the adsorption process is favored. The kinetics were monitored for 2 h by UV/Vis spectroscopy (MO peak at 465 nm, Shimadzu UV/Vis spectrophotometer UV-2600). Every 30 min an aliquot of 5 mL of dispersion was collected and filtrated using a 0.45 μm acetate cellulose microporous membrane. Then, UV/Vis spectra were registered for each aliquot (diluted 1:5 before measurement). The amount of MO adsorbed on the MnO$_2$ and MnO$_2$@AC40 during time (q$_t$, mg g^{-1}) was calculated using the following equation:

$$q_t = \frac{V(c_0 - c_t)}{W}$$

where c_0 and c_t (in mg L^{-1}) are the MO liquid phase concentrations at the initial and certain time t, respectively; V (in L) is the volume of the solution and W (g) is the mass of the adsorbent used.

Furthermore, in order to investigate the MO degradation mechanism, aliquots of methyl orange eluate (after 2 h) were examined by using HPLC-MS technique (HPLC Agilent Technologies 1200 series instrument coupled with a Thermo Scientific LTQ Orbitrap XL analyzer). Chromatographic separations were carried out on a Zorbax SB-C18 column (150 × 2.1 mm, particle size 3 μm), with a sample volume of 1 mL and a flux rate of 160 μL min^{-1}. The separation step was made using a mobile phase composed of a first component A (H$_2$O + HCOOH 0.1%) and a second component B (acetonitrile, AcN) in non-isocratic conditions: t = 0 min, A = 99% and B = 1%; t = 18 min, A = 10% and B = 90%. The stop time was fixed at 19 min. The chromatographic effluent was then ionized by nano-ESI in negative mode [M−H]$^{-}$. The ESI source settings were: spray voltage 2.5 kV; capillary temperature 250 °C. Mass spectrometric analyses were done in full scan mode (scan range 60.00–600.00 m/z).

The used MnO$_2$ powders were then investigated by Attenuated Total Reflectance Fourier Transformed Infrared (ATR-FTIR) spectroscopy to confirm both the MO adsorption and the possible by-products formation.

Finally, MO desorption from MnO$_2$ or MnO$_2$@AC40 powders was studied by adding NaOH (the suitable amount to increase the pH up to 10) in order to evaluate the adsorbent regeneration by analysing the UV/Vis spectra of the filtrated solutions.

3. Results and discussion

3.1. Physico-chemical characterizations of pure and carbon-based MnO$_2$ materials

The physico-chemical properties of all the prepared MnO$_2$ samples were finely tailored by varying the starting salt precursors/oxidizing agents.

From the morphological point of view, TEM images of each sample show sticky-shaped nanoparticles, having a diameter in the range 20–50 nm and lengths up to several hundred of nanometers (Fig. 1) [27,37]. Thus, the use of different synthetic reagents does

not seem to significantly influence the nanopowders morphology. Concerning the MS_Br@AC40 sample, the growth of manganese dioxide seems to provoke a perceivable change in the surface texture, since a more sponge-like structure could be appreciated by SEM technique with respect to the bare activated carbon (Fig. S1a and b). Furthermore, the effective presence of manganese onto carbon support (Fig. S1c and d) has been corroborated by EDX maps.

Instead, the structural analysis reveals a diversity in the polymorphic composition among the bare MnO$_2$. Indeed, MS_K sample is the only powder composed by the α phase, whereas all the other samples show the presence of a secondary polymorph, $i.e.$ β-ramsdellite one (Fig. S2, 2θ at around 22° and Table 2, 2nd column). Therefore, by keeping constant the manganese sulphate precursor and by varying the oxidizing agent, we evidenced the pivotal role played by both the cations and anions of the latter species. Actually, as already reported in the literature [27,39], the presence of K$^+$ ions (MS_K sample) favors the formation and growth of α-MnO$_2$ which is, by contrast, hindered by NH$_4^+$ (MS_N sample) that promotes the β-ramsdellite polymorph. The adoption of a third oxidant species ($i.e.$ KBrO$_3$, MS_Br nanopowder) has led to the same structural composition as in the case of MS_N. Indeed, notwithstanding the presence of potassium cations, the Br$_2$ gaseous molecules (deriving from bromate anions) could have inhibited the selective growth of the α-MnO$_2$ on behalf of the ramsdellite one (Fig. S2). Moreover, as concerns the adoption of manganese chloride instead of sulphate as the Mn^{2+} precursor, the formation of β-ramsdellite is probably due to the adsorption of Cl$^-$ ions which could hinder the growth of the α-phase along its preferential directions [37].

A further evaluation of the main role played by the adopted reagents was obtained by BET surface analysis. Once again, the use of the oxidants with potassium cations (in combination with manganese sulphate) has led to a higher value of S_{BET} ($e.g.$ 116 and 108 m^2 g^{-1} for MS_K and MS_Br, respectively; see Table 2, 3rd column) whereas the presence of NH$_4^+$ provoked a higher particle sintering degree [27,40], thus resulting in a lower surface area value (41 m^2 g^{-1}). On the contrary, the manganese chloride/potassium permanganate couple (MCl_K sample) has led to only 69 m^2 g^{-1} (Table 2). This fact is probably due to the presence of the chloride (instead of sulphate) anions that could remain adsorbed on the MnO$_2$ surface, promoting the sintering process and subsequently a lower surface area [37]. We also believe that SO$_4^{2-}$ groups (from sulphate Mn^{2+} precursor) and the surface —OH groups on the manganese oxide materials may interact with each other and form a steric barrier, thus preventing nanoparticles from further aggregation [37]. For MS_Br@AC40, a huge increase in the surface area has been observed with respect to MS_Br (Table 2, 4th and 7th lines), thanks to the carbon support (having a S_{BET} value of 1220 m^2 g^{-1}). Moreover, the growth of the oxide nanoparticles on it has led to the increase of the pores with diameter smaller than 20 nm (Table 2, 4th and 5th columns), which are pivotal for the final MO adsorption (see in the following). Further, the difference in the pore features can be clearly observed by analyzing the shape of the adsorption isotherms curves (Fig. S3). All the bare MnO$_2$ samples present an isotherm shape similar to type II, typical of mesoporous powders with slit-shaped pores opened at both ends and characterized by diameters larger than micropores [41]. On the contrary, the presence of the carbon support drastically changes the profile curve and the hysteresis loop into those typical of "bottle-neck" pores, $i.e.$ pores with a narrow opening and a wide body (according to McBain's theory) [41].

3.2. MO adsorption/degradation by pure and composite MnO$_2$ samples

3.2.1. MO adsorption capability by tailored MnO$_2$ nanopowders

The MO adsorption capacities of the different MnO$_2$ nanopowders have been evaluated by comparing the amount of dye mole-
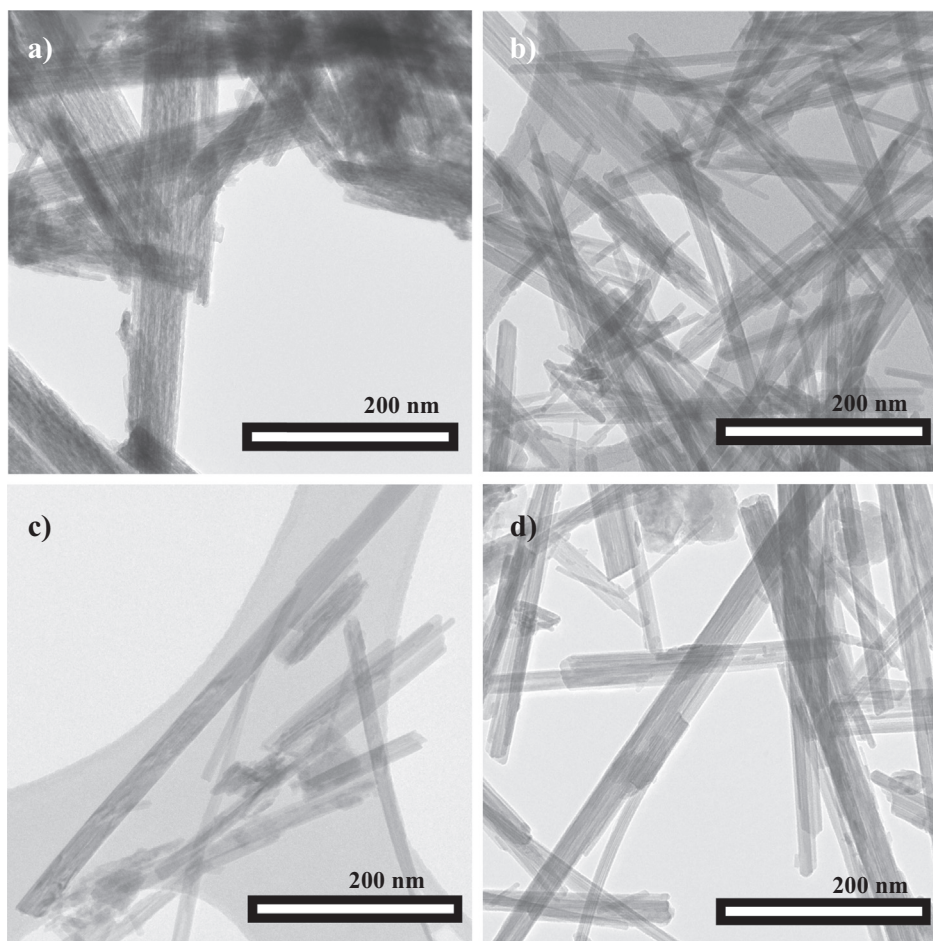
**Fig. 1.** TEM images of (a) MS_N, (b) MS_K, (c) MS_Br and (d) MCl_K.

Table 2
Physico-chemical features (*e.g.* XRPD polymorphic composition, surface area (S_{BET}), total pore volume ($V_{tot.\ pores}$) and relative percentages of pore size distribution) of both bare MnO_2 and carbon-based composite samples.

Sample	XRPD polymorph	S_{BET} (m^2 g^{-1})	$V_{tot.\ pores}$ (cm^3 g^{-1})	% d < 20 nm	% 20 < d < 80 nm	% d > 80 nm
MS_N	α + β	41	0.201	25	60	15
MS_K	α	116	0.895	8	74	18
MS_Br	α + β	108	0.430	30	53	17
MCl_K	α + β	69	0.576	13	71	16
AC40	–	1220	1.990	6	1	94
MS_Br@AC40	–	800	0.234	83	12	5

cules (q_t) adsorbed during time. Thus, among the pure MnO_2 samples MS_Br sample seems to be the most performing adsorbent material (Fig. 2), followed digressively by MS_N, MCl_K and MS_K powders. As widely known [9,28,42], the adsorption capability of a certain material is deeply connected with its surface features (*i.e.* the higher the surface area, the greater the adsorption performances). However, in this study, q_t (Fig. 2) values do not follow the S_{BET} trend (Table 2, 3rd column) since MS_K sample (S_{BET} = 116 m^2 g^{-1}) shows the worst adsorption behavior. According to the study reported by Liu et al. [43], the adsorption capacities could also depend on the MnO_2 crystallographic composition. Particularly, in our case, the growth of the secondary polymorph (β-ramsdellite, Table 2 and Fig. S2) seems to enhance the adsorbents performances. A further parallel explanation could be traced back to the total pore volume and the different pore size distribution (Table 2; from 4th to 7th column) of the tailor-made nanoparticles. Actually, methyl orange has a molecular size of around 26 Å in

aqueous solution [44], therefore powders with pore diameters nearly or larger than 30 Å could be filled by MO molecules. As it can be noticed in Table 2, MS_Br and MS_K samples have the highest and lowest percentages of pores with diameter under 20 nm, respectively [27]. Hence, this surface feature goes hand in hand with the adsorption capability, since smaller pores seem to promote the entrapment of the dye molecules, which is not guaranteed by a high percentage of bigger ones, due to the possible establishment of an adsorption/desorption equilibrium. Moreover, by comparing the IR spectra of both the synthesized nanopowders and MO, MnO_2 adsorbent performances previously observed have been corroborated. Indeed, some of the methyl orange characteristic peaks (highlighted in the MO spectrum of Figs. S3 and S4, *e.g.* stretching of C=C (1599 cm^{-1}), S=O (1115 cm^{-1} and 1035 cm^{-1}), C=N (1313 cm^{-1}) and N=N (1519 cm^{-1}), and bending of C—C (1193 cm^{-1}) and C—H (750–800 cm^{-1}) [28,43,45]) are still present in the spectra of used MS_N, MCl_K and MS_Br samples. On the
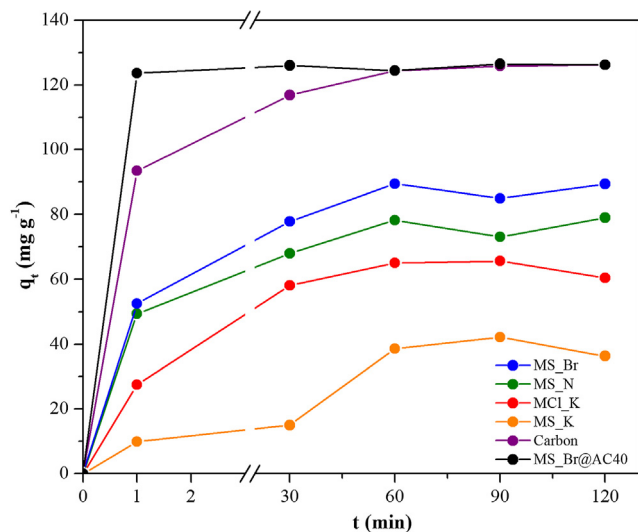
Fig. 2. Effect of contact time on the adsorption capability (q_t) of all the samples, both pure and composite one. Experimental conditions: 100 mg L^{-1} of initial MO, 75 mg of the adsorbent powder, total volume of 150 mL and T = (293 ± 1) K.

contrary, there is no peaks evidence for MS_K, thus underlining again its lowest adsorption capacity.

3.2.2. MO adsorption capability by MS_Br@AC40 composite

Once figured out MS_Br could lead to a significant MO removal, to further enhance its performances we decided to grow it onto Activated Carbon pellets, which are easier to remove and have a very high surface area (1220 m^2 g^{-1}, Table 2). Hence, MO removal tests have been carried out with the achievement of almost the total dye disappearance within the very first minutes of the adsorption kinetics (Fig. 2, purple line). Moreover, we succeeded in demonstrating the optimal synergistic effect between MS_Br and the carbon support, since the highest q_t values were obtained by MS_Br@AC40 sample. This may be due to the high active surface area of AC40 (with a desired porosity, Table 2) along with the possible degradation/oxidation power of MnO$_2$ nanoparticles. This is fully in accordance with the results of Xu and co-workers [31], who reported that the three-dimensional MnO$_2$/Carbon sphere composite has an outstanding Hg^0 removal performance, due to either its higher catalytic oxidation or adsorption capability.

Further, in order to corroborate the present hypothesis, higher MS_Br amounts were considered (by keeping constant the MO concentration) and the UV/Vis spectra of the corresponding eluates (after 2 h of kinetic process) have been recorded. Fig. S5 interestingly shows the shifting of MO characteristic peak towards lower wavelength values (*i.e.* from 465 to 350 nm), in the case of high MS_Br amount (>75 mg). Thus, we believe that this fact could be ascribable to the possible modification of the methyl orange molecules, particularly to the formation of MO by-products.

Moreover, an electrochemical characterization of the prepared MS_Br sample has been performed. We have evidenced the presence of several peaks referable to different Mn oxidation states (*i.e.* MnOOH, Mn^{3+}, Mn^{2+}, MnO$_2$, Mn$_3$O$_4$, Fig. 3a), according to studies already reported in the literature [46,47]. Hence defective MnO$_2$ lattice, characterized by different manganese oxidation states (namely Mn$^{\delta+}$), can be hypothesized, which are also confirmed by X-ray Photoelectron Spectroscopy (XPS) analyses as shown in Fig. 3b (for MS_Br as representative sample). Therefore, the existence of Mn$^{\delta+}$ (with valence higher than IV) species may assure a strong oxidizing power. For this reason, methyl orange could undergo a chemical degradation process only due to the presence
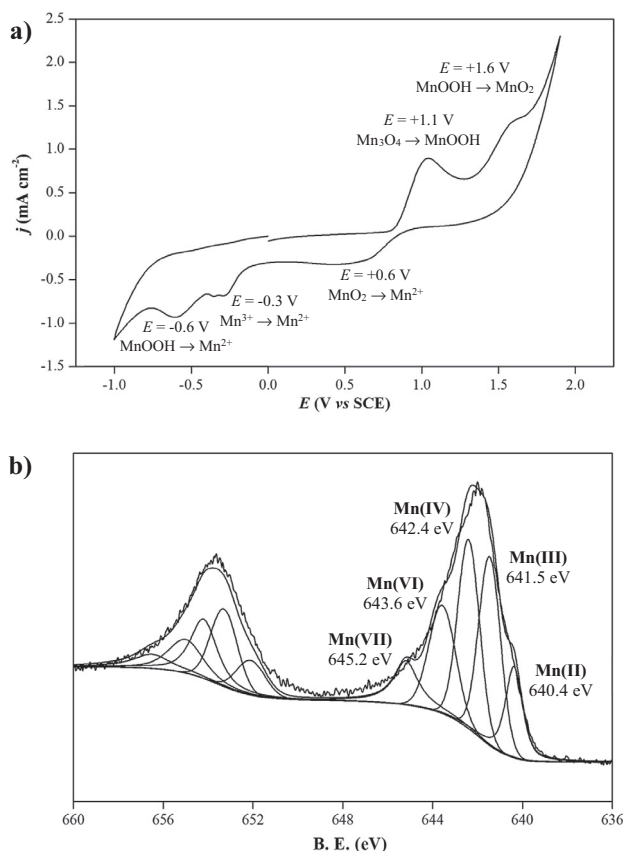
Fig. 3. (a) Cyclic voltammetric curve for MS_Br–GC sample (as representative one) recorded in AcONa/AcOH buffer. The main CV peaks have been attributed to different Mn species, according to the literature [46,47]; (b) Mn 2p fitted XP spectrum relative to MS_Br.

of nano-MnO$_2$, without any advanced oxidation promoter (*i.e.* Fenton reagent or H$_2$O$_2$) or any kind of activation energy (such as the UV light).

3.2.3. The proposed MO degradation mechanism

HPLC-MS analyses on eluates at the end of the kinetic tests by using both MS_Br and MS_Br@AC40 absorbents have been performed, in order to study the MO removal mechanism and the recognition of the possible by-products. Fig. 4 shows the extracted [M−H]$^-$ ion chromatograms relative to the HPLC-MS detected species. The methyl orange peak has been observed (MO, m/z 305.03, 14.3 min Retention Time (RT)), confirming that some of the starting dye molecules remain without undergoing a degradation phenomenon. Further, several by-products were detected: (i) A (m/z 291.10, 15.7 min RT); (ii) B (m/z 277.09, 14.2 min RT); (iii) C (m/z 155.00, 2.9 min RT); and (iv) D (m/z 141.01, 2.7 min RT). Although the mass spectrometry analysis should not be considered as a quantitative study, the relevant abundance of the different [M−H]$^-$ intermediates was determined in order to evaluate their variation during the reaction time (both at half – 30 min – and at the end – 120 min – of the removal tests; Table 3). As observed previously, notwithstanding the MS_Br powder is the most performing one among the MnO$_2$ materials, after 2 h, a great amount of the starting MO molecule and by-products with high m/z values (A and B molecules) still remains at the end of the reaction. However, this behavior confirms the hypothesis that MS_Br sample could act not only as an adsorbent but also as a catalytic oxidant towards the pollutant species. Furthermore, the almost complete degradation power of MS_Br@AC40 sample leading to the very low presence of the
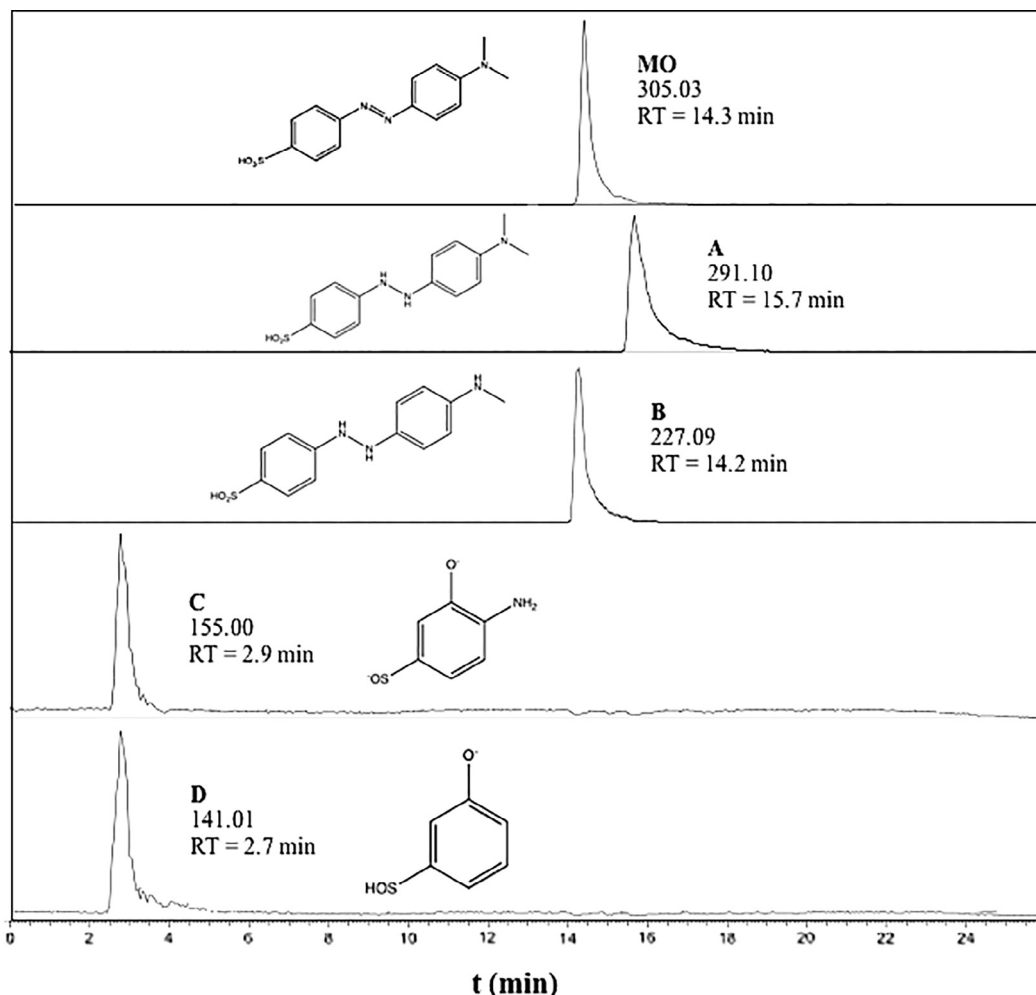
Fig. 4. Extracted [M−H]⁻ ion chromatograms after 30 min of MO adsorption kinetic for MS_Br, AC40 and MS_Br@AC40 powders.

Table 3
HPLC-MS methyl orange (MO) and intermediates abundance after 30 and 120 min of adsorption/degradation tests (legend: +++ > 3 · 10^8, ++ = 10^8, + = 10^7, o = 10^6, t = 10^5, − = none).

Sample	After 30 min					After 120 min				
	MO (305 m/z)	A (291 m/z)	B (277 m/z)	C (155 m/z)	D (141 m/z)	MO (305 m/z)	A (291 m/z)	B (277 m/z)	C (155 m/z)	D (141 m/z)
MS_Br	++	+++	++	+	+	++	+++	++	+	+
Carbon	++	+++	+	t	t	o	+	t	t	t
MS_Br@AC40	t	o	t	−	+	t	o	t	−	−

starting MO and by-products, even with the lower molecular weights (C and D, either after 30 or 120 min; Table 3), is clearly evident. On the contrary, as concerns the AC40, the scarce amount of intermediates allows us to consider it as only an adsorbent material. Hence, since we obtained different results for pure carbon and MS_Br@AC40, we demonstrate once again the synergistic effect between AC and MnO_2 nanoparticles.

Thus, Fig. 5 shows the possible MO degradation path observed by exploiting both MS_Br and MS_Br@AC40 samples. Several steps could be hypothesized: (i) the reduction of the sulfonic moiety to the sulfenic one; (ii) the oxidation followed by the cleavage of the azo-bond; (iii) the loss of the amine group and (iv) the addition of a hydroxyl group to the phenyl ring. No other species characterized by lower m/z values have been detected.

3.2.4. Adsorbent regeneration

The last part of the present work was focused on the possible reuse of the pure and composite MnO_2 absorbents. Indeed, we saw that a pH shift towards alkaline values (up to ∼10) could provoke a reversible desorption of both pristine MO species together with possible MO by-products. The investigated carbon-based samples (AC40 and MS_Br@AC40) seem to have good regeneration properties, since the q_t trend (Fig. 6a) resembles the one obtained before the MO adsorption tests (see Fig. 2); whereas, in the case of pure MS_Br, a drastic decrease in the removal properties has been observed. Furthermore, UV/Vis spectra of eluates after regeneration show well-pronounced peaks shifted towards lower wavelengths for MS_Br and MS_Br@AC40 adsorbents, probably due to by-products adsorption. On the contrary, the absorbance
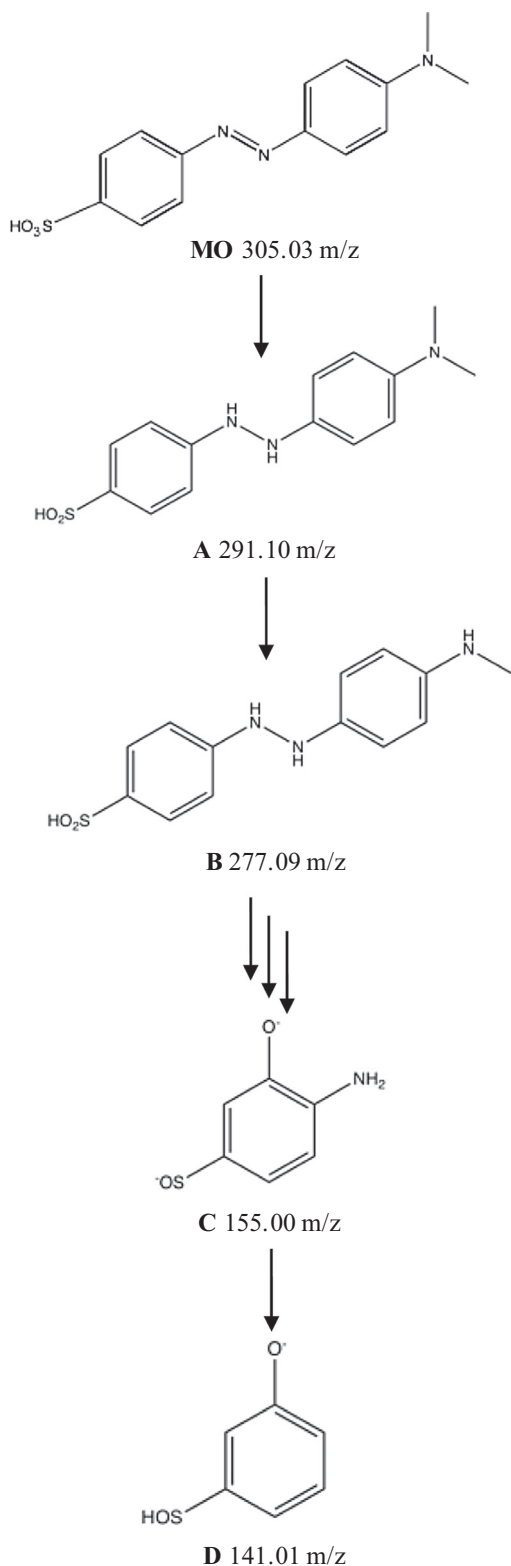
MO 305.03 m/z

A 291.10 m/z

B 277.09 m/z

C 155.00 m/z

D 141.01 m/z

Fig. 5. Hypothesis of the possible MO degradation pathway based on HPLC-MS results.

Fig. 6. (a) Adsorption capability (q_t) trend after powders regeneration; (b) UV/Vis spectra of MO eluate, before and after the powder regeneration treatment with NaOH.

4. Conclusions

In the present research work, we dealt with the syntheses of both pure and carbon-supported manganese dioxide nanoparticles, which showed great adsorbent/oxidative properties towards aqueous methyl orange pollutant molecules.

Hence, by varying both the manganese salt precursors (*e.g.* sulphate or chloride) and the oxidizing agents (*e.g.* ammonium persulphate, potassium permanganate or potassium bromate), we succeeded in modulating the structural, morphological and surface features of the final MnO_2 nanopowders. Particularly, all the nanoparticles show a nanorod-like morphology and diverse polymorphic composition. In the case of manganese sulphate/potassium permanganate coupling (MS_K sample), XRPD analysis showed peaks ascribable only to the α-phase; whereas all the other powders are also composed by the β-ramsdellite one. Thus, the presence of the latter, along with a higher percentage of pores with diameter under 20 nm seemed to favor the dye removal. Hence, MS_Br sample (that matches all these properties) revealed to be the most performing adsorbent. Subsequently, studies on the most suitable MnO_2 concentration were carried out, obtaining an optimal 5:1 weight proportion between MS_Br and MO molecule. This powder then was grown on Activated Carbon (AC) pellets to either enhance its removal properties or to facilitate the adsorbent removal at the end of the kinetic test. By means of HPLC-MS analysis on eluates (after 2 h of the adsorption kinetic), we also

of the eluate from AC40 regeneration is flat, therefore underlining either its superior MO adsorption capability and the negligible releasing properties. Hence, MS_Br@AC40 seems to represent a significant step forward to the unmodified exploited activated carbon.
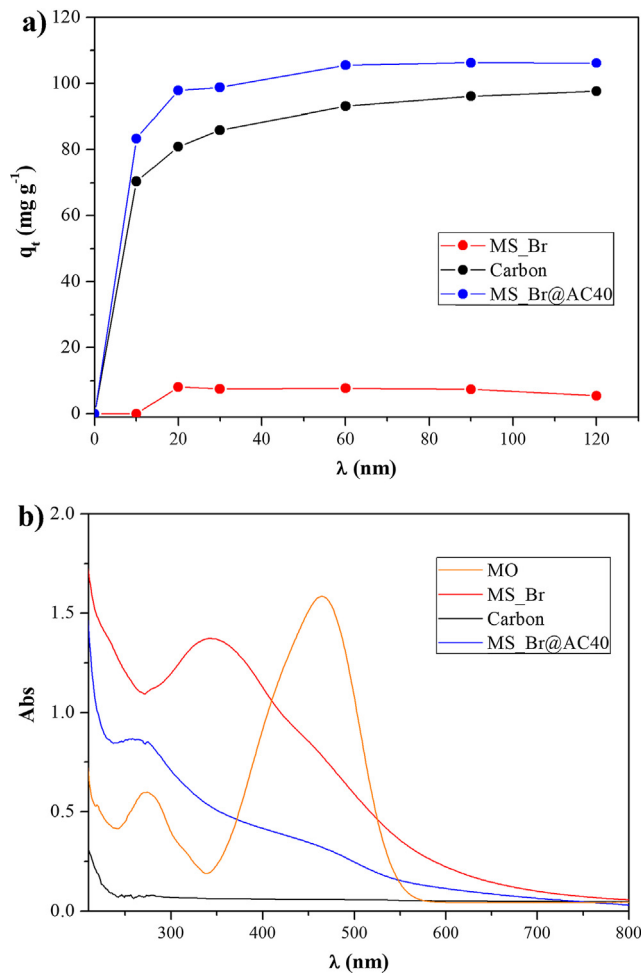
investigated the MS_Br and MnO₂@AC40 degradative power towards MO molecules, thus leading to a novel degradation pathway. Hence, MnO₂@AC40 composite seems to exhibit the optimal properties in degrading/adsorbing the MO molecules.

Finally, the adsorbent regeneration capability has been evaluated by shifting the pH of the aqueous adsorbent/MO system towards alkaline values (around 10). Promising results, in terms of complete reusability, were obtained, especially for MS_Br@AC40 powder.

Conflict of interest

The authors declare that there is no conflict of interest regarding the publication of this paper.

Appendix A. Supplementary material

Supplementary data associated with this article can be found, in the online version, at https://doi.org/10.1016/j.apsusc.2018.03.170.

References

[1] E. Paoli, G. Cappelletti, L. Falciola, Electrochemistry as a tool for nano-TiO₂ deposition and for photoremediation pollutant monitoring, Electrochem. Commun. 12 (2010) 1013–1016, https://doi.org/10.1016/j.elecom.2010.05.012.

[2] C. Pirola, C.L. Bianchi, S. Gatto, S. Ardizzone, G. Cappelletti, Pressurized photoreactor for the degradation of the scarcely biodegradable DPC cationic surfactant in water, Chem. Eng. J. 225 (2013) 416–422, https://doi.org/10.1016/j.cej.2013.03.116.

[3] A. Colombo, G. Cappelletti, S. Ardizzone, I. Biraghi, C.L. Bianchi, D. Meroni, C. Pirola, F. Spadavecchia, Bisphenol A endocrine disruptor complete degradation using TiO₂ photocatalysis with ozone, Environ. Chem. Lett. 10 (2012) 55–60, https://doi.org/10.1007/s10311-011-0328-0.

[4] J. Kim, Y. Park, H. Park, Solar hydrogen production coupled with the degradation of a dye pollutant using TiO₂ modified with platinum and nafion, Int. J. Photoenergy 2014 (2014) 1–9, https://doi.org/10.1155/2014/324859.

[5] C.A. Martínez-Huitle, E. Brillas, Decontamination of wastewaters containing synthetic organic dyes by electrochemical methods: a general review, Appl. Catal. B Environ. 87 (2009) 105–145, https://doi.org/10.1016/j.apcatb.2008.09.017.

[6] T.-D. Dang, A.N. Banerjee, Q.-T. Tran, S. Roy, Fast degradation of dyes in water using manganese-oxide-coated diatomite for environmental remediation, J. Phys. Chem. Solids 98 (2016) 50–58, https://doi.org/10.1016/j.jpcs.2016.06.006.

[7] Y.-P. Chen, S.-Y. Liu, H.-Q. Yu, H. Yin, Q.-R. Li, Radiation-induced degradation of methyl orange in aqueous solutions, Chemosphere 72 (2008) 532–536, https://doi.org/10.1016/j.chemosphere.2008.03.054.

[8] V.K. Gupta, I. Ali, T.a. Saleh, A. Nayak, S. Agarwal, Chemical treatment technologies for waste-water recycling – an overview, RSC Adv. 2 (2012) 6380. http://doi.org/10.1039/c2ra20340e.

[9] Y. Liu, C. Luo, J. Sun, H. Li, Z. Sun, S. Yan, Enhanced adsorption removal of methyl orange from aqueous solution by nanostructured proton-containing δ-MnO₂, J. Mater. Chem. A 3 (2015) 5674–5682, https://doi.org/10.1039/C4TA07112C.

[10] H. Bai, P. He, J. Chen, K. Liu, H. Lei, F. Dong, X. Zhang, H. Li, Fabrication of Sc₂O₃-magneli phase titanium composite electrode and its application in efficient electrocatalytic degradation of methyl orange, Appl. Surf. Sci. 401 (2017) 218–224, https://doi.org/10.1016/j.apsusc.2017.01.019.

[11] G. Huang, Y. Sun, C. Zhao, Y. Zhao, Z. Song, J. Chen, S. Ma, J. Du, Z. Yin, Water–n-BuOH solvothermal synthesis of ZnAl–LDHs with different morphologies and its calcined product in efficient dyes removal, J. Colloid Interface Sci. 494 (2017) 215–222, https://doi.org/10.1016/j.jcis.2017.01.079.

[12] Y. Chen, J. Peng, H. Xiao, H. Peng, L. Bu, Z. Pan, Y. He, F. Chen, X. Wang, S. Li, Adsorption behavior of hydrotalcite-like modified bentonite for Pb²⁺, Cu²⁺ and methyl orange removal from water, Appl. Surf. Sci. 420 (2017) 773–781, https://doi.org/10.1016/j.apsusc.2017.05.138.

[13] J. Chen, X. Shi, Y. Zhan, X. Qiu, Y. Du, H. Deng, Construction of horizontal stratum landform-like composite foams and their methyl orange adsorption capacity, Appl. Surf. Sci. 397 (2017) 133–143, https://doi.org/10.1016/j.apsusc.2016.10.211.

[14] Y. Tian, H. Li, Z. Ruan, G. Cui, S. Yan, Synthesis of NiCo₂O₄ nanostructures with different morphologies for the removal of methyl orange, Appl. Surf. Sci. 393 (2017) 434–440, https://doi.org/10.1016/j.apsusc.2016.10.053.

[15] J.P. Guin, Y.K. Bhardwaj, L. Varshney, Mineralization and biodegradability enhancement of Methyl Orange dye by an effective advanced oxidation process, Appl. Radiat. Isot. (2017), https://doi.org/10.1016/j.apradiso.2017.01.018.

[16] H.-T. Ren, Q. Yang, Fabrication of Ag₂O/TiO₂ with enhanced photocatalytic performances for dye pollutants degradation by a pH-induced method, Appl. Surf. Sci. 396 (2017) 530–538, https://doi.org/10.1016/j.apsusc.2016.10.191.

[17] S. Qin, Y. Liu, Y. Zhou, T. Chai, J. Guo, Synthesis and photochemical performance of CdS nanoparticles photocatalysts for photodegradation of organic dye, J. Mater. Sci. Mater. Electron. (2017), https://doi.org/10.1007/s10854-017-6453-1.

[18] N. Al-Bastaki, Removal of methyl orange dye and Na₂SO₄ salt from synthetic waste water using reverse osmosis, Chem. Eng. Process. Process Intensif. 43 (2004) 1561–1567, https://doi.org/10.1016/j.cep.2004.03.001.

[19] M.H. Dehghani, B. Karimi, M.S. Rajaei, The effect of aeration on advanced coagulation, flotation and advanced oxidation processes for color removal from wastewater, J. Mol. Liq. 223 (2016) 75–80, https://doi.org/10.1016/j.molliq.2016.08.019.

[20] D. Zhao, W. Zhang, C. Chen, X. Wang, Adsorption of methyl orange dye onto multiwalled carbon nanotubes, Proc. Environ. Sci. 18 (2013) 890–895, https://doi.org/10.1016/j.proenv.2013.04.120.

[21] R. Huang, Q. Liu, J. Huo, B. Yang, Adsorption of methyl orange onto protonated cross-linked chitosan, Arab. J. Chem. 10 (2017) 24–32, https://doi.org/10.1016/j.arabjc.2013.05.017.

[22] J. Pang, Q. Han, W. Liu, Z. Shen, X. Wang, J. Zhu, Two basic bismuth nitrates: [Bi₆O₆(OH)₂](NO₃)₄·2H₂O with superior photodegradation activity for rhodamine B and [Bi₆O₅(OH)₃](NO₃)₅·3H₂O with ultrahigh adsorption capacity for methyl orange, Appl. Surf. Sci. 422 (2017) 283–294, https://doi.org/10.1016/j.apsusc.2017.06.022.

[23] H. Tang, H. Huang, X. Wang, K. Wu, G. Tang, C. Li, Hydrothermal synthesis of 3D hierarchical flower-like MoSe₂ microspheres and their adsorption performances for methyl orange, Appl. Surf. Sci. 379 (2016) 296–303, https://doi.org/10.1016/j.apsusc.2016.04.086.

[24] S.A. Hassanzadeh-Tabrizi, M.M. Motlagh, S. Salahshour, Synthesis of ZnO/CuO nanocomposite immobilized on γ-Al₂O₃ and application for removal of methyl orange, Appl. Surf. Sci. 384 (2016) 237–243, https://doi.org/10.1016/j.apsusc.2016.04.165.

[25] M. Wiśniewska, A. Nosal-Wiercińska, I. Ostolska, D. Sternik, P. Nowicki, R. Pietrzak, A. Bazan-Wozniak, O. Goncharuk, Nanostructure of poly(acrylic acid) adsorption layer on the surface of activated carbon obtained from residue after supercritical extraction of hops, Nanoscale Res. Lett. 12 (2017) 2, https://doi.org/10.1186/s11671-016-1772-3.

[26] A. Minguzzi, G. Longoni, G. Cappelletti, E. Pargoletti, C. Di Bari, C. Locatelli, M. Marelli, S. Rondinini, A. Vertova, The influence of carbonaceous matrices and electrocatalytic MnO₂ nanopowders on lithium-air battery performances, Nanomaterials 6 (2016), https://doi.org/10.3390/nano6010010.

[27] E. Pargoletti, G. Cappelletti, A. Minguzzi, S. Rondinini, M. Leoni, M. Marelli, A. Vertova, High-performance of bare and Ti-doped α-MnO₂ nanoparticles in catalyzing the Oxygen Reduction Reaction, J. Power Sources 325 (2016) 116–128, https://doi.org/10.1016/j.jpowsour.2016.06.020.

[28] H.H. Peng, J. Chen, D.Y. Jiang, M. Li, L. Feng, D. Losic, F. Dong, Y.X. Zhang, Synergistic effect of manganese dioxide and diatomite for fast decolorization and high removal capacity of methyl orange, J. Colloid Interface Sci. 484 (2016) 1–9, https://doi.org/10.1016/j.jcis.2016.08.057.

[29] M. Ramesh, H.S. Nagaraja, M.P. Rao, S. Anandan, N.M. Huang, Fabrication, characterization and catalytic activity of α-MnO₂ nanowires for dye degradation of reactive black 5, Mater. Lett. 172 (2016) 85–89, https://doi.org/10.1016/j.matlet.2016.02.076.

[30] H. Xu, J. Xie, Y. Ma, Z. Qu, S. Zhao, W. Chen, W. Huang, N. Yan, The cooperation of FeSn in a MnOx complex sorbent used for capturing elemental mercury, Fuel 140 (2015) 803–809, https://doi.org/10.1016/j.fuel.2014.10.004.

[31] H. Xu, J. Jia, Y. Guo, Z. Qu, Y. Liao, J. Xie, W. Shangguan, N. Yan, Design of 3D MnO₂/carbon sphere composite for the catalytic oxidation and adsorption of elemental mercury, J. Hazard. Mater. 342 (2018) 69–76, https://doi.org/10.1016/j.jhazmat.2017.08.011.

[32] M.A. Al-Ghouti, Y.S. Al-Degs, A.A. Issa, R.Z. Al Bakain, M.A. Khraisheh, Mechanistic and adsorption equilibrium studies of dibenzothiophene-rich-diesel on MnO₂-loaded-activated carbon: surface characterization, Environ. Prog. Sustain. Energy 36 (2017) 903–913, https://doi.org/10.1002/ep.12539.

[33] J.-W. Wang, Y. Chen, B.-Z. Chen, A synthesis method of MnO₂/activated carbon composite for electrochemical supercapacitors, J. Electrochem. Soc. 162 (2015) A1654–A1661, https://doi.org/10.1149/2.0031509jes.

[34] G. Soliveri, V. Piferi, G. Panzarasa, S. Ardizzone, G. Cappelletti, D. Meroni, K. Sparnacci, L. Falciola, Self-cleaning properties in engineered sensors for dopamine electroanalytical detection, Analyst 140 (2015) 1486–1494, https://doi.org/10.1039/C4AN02219J.

[35] G. Di Liberto, V. Pifferi, L. Lo Presti, M. Ceotto, L. Falciola, Atomistic explanation for interlayer charge transfer in metal-semiconductor nanocomposites: the case of silver and anatase, J. Phys. Chem. Lett. 8 (2017) 5372–5377, https://doi.org/10.1021/acs.jpclett.7b02555.

[36] G. Cappelletti, P. Fermo, M. Camiloni, Smart hybrid coatings for natural stones conservation, Prog. Org. Coat. 78 (2015) 511–516, https://doi.org/10.1016/j.porgcoat.2014.05.029.

[37] S. Orsini, E. Pargoletti, A. Vertova, A. Minguzzi, C. Locatelli, S. Rondinini, G. Cappelletti, Ad hoc tailored electrocatalytic MnO_2 nanorods for the oxygen reduction in aqueous and organic media, J. Electroanal. Chem. 808 (2018) 439–445, https://doi.org/10.1016/j.jelechem.2017.05.035.

[38] G.S. Patterson, A simplified method for finding the pKa of an acid-base indicator by spectrophotometry, J. Chem. Educ. 76 (1999) 395, https://doi.org/10.1021/ed076p395.

[39] X. Huang, D. Lv, H. Yue, A. Attia, Y. Yang, Controllable synthesis of α- and β-MnO_2: cationic effect on hydrothermal crystallization, Nanotechnology 19 (2008) 225606, https://doi.org/10.1088/0957-4484/19/22/225606.

[40] L. Benhaddad, L. Makhloufi, B. Messaoudi, K. Rahmouni, H. Takenouti, Reactivity of nanostructured MnO_2 in alkaline medium studied with a microcavity electrode: effect of oxidizing agent, J. Mater. Sci. Technol. 27 (2011) 585–593.

[41] S. Lowell, Introduction to Powder Surface Area, John Wiley and Sons, 1979.

[42] E. Khosla, Adsorption of azo dye methyl orange over aluminum oxide nano particles, Int. J. Basic Appl. Chem. Sci. 5 (2015) 37–46.

[43] Y. Liu, J. Wei, Y. Tian, S. Yan, The structure–property relationship of manganese oxides: highly efficient removal of methyl orange from aqueous solution, J. Mater. Chem. A 3 (2015) 19000–19010, https://doi.org/10.1039/C5TA05507E.

[44] M. Danish, R. Hashim, M.N.M. Ibrahim, O. Sulaiman, Characterization of physically activated *Acacia mangium* wood-based carbon for the removal of methyl orange dye, BioResources 8 (2013) 4323–4339, https://doi.org/10.15376/biores.8.3.4323-4339.

[45] R. Nandini, B. Vishalakshi, A study of interaction of methyl orange with some polycations, E-J. Chem. 9 (2012) 1–14, https://doi.org/10.1155/2012/343928.

[46] A. Salimi, B. Pourbahram, S. Mansouri-Majd, R. Hallaj, Manganese oxide nanoflakes/multi-walled carbon nanotubes/chitosan nanocomposite modified glassy carbon electrode as a novel electrochemical sensor for chromium (III) detection, Electrochim. Acta 156 (2015) 207–215, https://doi.org/10.1016/j.electacta.2014.12.146.

[47] A.-M. Gurban, D. Burtan, L. Rotariu, C. Bala, Manganese oxide based screen-printed sensor for xenoestrogens detection, Sens. Actuat. B Chem. 210 (2015) 273–280, https://doi.org/10.1016/j.snb.2014.12.111.